nature communications

Article

https://doi.org/10.1038/s41467-025-60365-5

Structure and assembly of the MmpL5/MmpS5 efflux transporter from *Mycobacterium tuberculosis*

Received: 10 June 2024

Accepted: 21 May 2025

Zhiqi Xiong[1,2], Xiaolin Yang[3], Shule Wang[1], Caitlan J. Smart[4], Hazel M. Sisson[4], Zhenli Lin[1], Tianyu Hu[1], Yuting Ran[1], Chuyao Xu[1], Xiuna Yang[1,5], Yao Zhao[3], William J. Jowsey[4], Gregory M. Cook[4,6], Matthew B. McNeil[4], Luke W. Guddat[7], Zihe Rao[1,2] & Bing Zhang[1]

The MmpL5/MmpS5 efflux system in *Mycobacterium tuberculosis* plays crucial roles in extruding therapeutic drugs (*e.g.*, bedaquiline), and exporting siderophores (*i.e.*, (carboxy)mycobactins). However, the molecular basis underlying these processes remains unknown due to the lack of structural information. Here, we report the cryo-electron microscopy structures of *Mycobacterium tuberculosis* MmpL5/MmpS5 at resolutions ranging from 2.64 to 3.31 Å, revealing it to be a trimer. The core of this complex is formed by three MmpL5 subunits assembled in a unique shoulder-to-shoulder ring-like configuration, with each MmpS5 subunit positioned between the two adjacent MmpL5 subunits. A remarkable feature of this system is the extracellular stalk, which spans approximately 130 Å in length and is composed of three intertwined anti-parallel coiled-coil portions of MmpL5. The stalk secures the tight association of the three MmpL5 subunits and exhibits intrinsic structural flexibility. Additionally, an unexpected MmpL5 binder, AcpM, a mycobacterial acyl carrier protein, has also been identified. Collectively, the study provides insights into the biological assembly and molecular function of MmpL5/MmpS5, which will facilitate the discovery of innovative inhibitors for this system.

Drug resistance in *Mycobacterium tuberculosis* (*Mtb*) is a significant problem for the effective treatment of tuberculosis (TB)[1,2], with multiple mechanisms making contributions[3–7], including the highly impermeable cell wall, mutations to target genes, antibiotic modification or degradation, and the action of efflux pumps. The role of efflux pumps, particularly the MmpL5/MmpS5 system, is emerging as a significant factor in *Mtb* drug resistance, especially considering its involvement in the clinical tolerance of bedaquiline (BDQ) and clofazimine (CFZ)[8–10], two drugs currently used to treat drug-resistant tuberculosis (DR-TB).

BDQ, the first FDA-approved anti-TB drug in over 40 years, targets subunit C of the ATP synthase encoded by the *atpE* gene[11–14]. However, cases of BDQ treatment failure have been reported[15–18], with resistance linked to efflux pumps rather than site-of-action changes to the target,

---

[1]Shanghai Institute for Advanced Immunochemical Studies and School of Life Science and Technology, ShanghaiTech University, Shanghai, China. [2]Laboratory of Structural Biology, School of Basic Medical Sciences, Tsinghua University, Beijing, China. [3]National Clinical Research Center for Infectious Disease, Shenzhen Third People's Hospital, Shenzhen, China. [4]Department of Microbiology and Immunology, University of Otago, Dunedin, New Zealand. [5]Shanghai Clinical Research and Trial Center, Shanghai, China. [6]School of Biomedical Sciences, Queensland University of Technology, Translational Research Institute, Woolloongabba, QLD, Australia. [7]School of Chemistry and Molecular Biosciences, The University of Queensland, Brisbane, QLD, Australia. e-mail: raozh@mail.tsinghua.edu.cn; zhangbing@shanghaitech.edu.cn

AtpE[9,19,20]. Many clinically observed variants occur in the *Rv0678* gene, encoding a transcriptional repressor protein MmpR5 that regulates the expression level of the MmpL5/MmpS5 efflux system[20–26]. These variants upregulate the expression of MmpL5/MmpS5, enhancing the ability of *Mtb* to efflux BDQ[8]. Moreover, upregulation of MmpL5/MmpS5 also augments clinical resistance to CFZ, a repurposed drug for DR-TB treatment[27,28].

The physiological function of bacterial efflux pumps is not inherently to transport antibiotics, and this is certainly the case with the MmpL5/MmpS5 system[29]. The MmpL5/MmpS5 and MmpL4/MmpS4 systems are responsible for exporting siderophores, specifically (carboxy)mycobactins, to scavenge iron from host proteins[30]. This process is crucial for the survival and pathogenicity of *Mtb* within the host[30], as iron is an essential element for mycobacterial metabolism and virulence[30,31]. However, the molecular details of how this system extrudes drugs and siderophores remain unknown.

In the MmpL5/MmpS5 system, MmpL5 is a predicted resistance-nodulation-division (RND) superfamily transporter, which is powered by the proton-motive force[32]. The periplasmic adapter protein MmpS5, co-encoded with MmpL5 in an operon, is integrated into the cell membrane via its N-terminal single transmembrane helix[33]. MmpS5 has also been shown to play a role in the oligomerization of MmpL5 and is essential for its function[30,34]. Yet, little is known about how the biological assembly between MmpL5 and MmpS5 is constructed, as well as the exact function of MmpS5.

Beyond MmpL5, the *Mtb* genome harbors 12 virulence-related MmpL (*M*ycobacterial *m*embrane *p*rotein *L*arge) proteins[33], all members of the RND protein superfamily[35]. Phylogenetic analysis divides these MmpL proteins into two distinct clusters with similar topologies[36]. Notably, structural predictions have revealed a striking feature of Cluster I MmpL proteins, including MmpL5: their extracellular regions contain a long anti-parallel coiled-coil structure (Supplementary Fig. 1), which is not found in any other characterized RND protein. Moreover, MmpL3 from Cluster II appears to function as a monomer[37,38], whereas the functional forms of the 10 members in Cluster I remain enigmatic due to the absence of structural information.

Here, we describe a high-resolution structure of the *Mtb* MmpL5/MmpS5 efflux transporter using single-particle cryo-electron microscopy (cryo-EM) analysis. These structural insights provide an unprecedented and detailed perspective on the biological assembly and molecular function of this pivotal efflux transporter and associated MmpL proteins.

Results

Structure determination

To elucidate the molecular architecture of the MmpL5/MmpS5 efflux system, we cloned the *Mtb mmpS5-mmpL5* (*Rv0677c-Rv0676c*) gene into the pMV261 vector, where the C-terminus of MmpL5 is attached to a 1×FLAG-tag, and then expressed in *Mycobacterium smegmatis* (*M. smegmatis*) strain mc^{2}155. The isolated MmpL5/MmpS5 exhibited a variety of oligomeric species in solution, as evidenced by SDS-PAGE, BN-PAGE and mass spectrometry (MS) (Supplementary Fig. 2), suggesting this transporter is dynamic in nature. The highest molecular mass species obtained from gel filtration chromatography that was homogeneous, was selected for analysis using single particle cryo-EM (Supplementary Fig. 2). The composite 2.84 Å resolution map (map-1) calculated without imposed symmetry revealed three similar protomers interacting closely as a trimeric structure (Supplementary Fig. 3). We then generated an improved EM map (map-2) with an overall resolution of 2.64 Å by imposing C3 symmetry. It is noteworthy that an unusual feature observed in the two-dimensional class averages was a weaker, elongated density that most likely corresponds to the quaternary structure composed of the coiled-coil part of MmpL5 (Supplementary Fig. 3b). Thus, we refer to this periplasmic region as the "stalk" of the complex. However, this structure was not observed in the composite map, speculating that the poor density is the result of the movement of the stalk relative to other parts. In the subsequent three-dimensional classification, we unexpectedly observed an initial map reconstructed by a minor population of particles, where the clear feature of the stalk emerged. We reconstructed this density map (map-3) at an overall resolution of 3.31 Å in C1 symmetry using a total of 10,751 particles (Supplementary Fig. 3c). Map-3 shows an almost intact stalk, but the quality of this part is poor. The overall resolution of map-3 was improved to 2.95 Å by enforcing C3 symmetry (map-4), yet the EM density of the stalk remained uninterpretable, especially its terminus, that is deteriorated, suggesting the intrinsic flexibility and complexity of this stalk.

The densities permitted the unambiguous assignment of the MmpL5 and MmpS5 subunits (Supplementary Fig. 4). However, only the density for the ordered transmembrane helices (residues: 1–34) of MmpS5 was observed (Supplementary Fig. 4e), whereas the extracellular domain (residues: 35–142) was invisible in the cryo-EM maps. Furthermore, the density for the stalk formed by the coiled-coil regions of MmpL5 (residues: 503–668) is too weak to assign secondary structure, although a predicted stalk model correlated well with the density envelope (Supplementary Fig. 4d). Unexpectedly, additional protein-like densities tightly bound to the cytoplasmic surface of each MmpL5 molecule were detected in the reconstructed EM map (Fig. 1a). With the aid of a structure-based search utilizing a PolyA model derived from the density map, the unknown protein was identified as the *M. smegmatis* acyl carrier protein, AcpM (MSMEG_4326) (Supplementary Fig. 4f). This analysis was further confirmed by MS analysis (Supplementary Fig. 2e). In addition, large numbers of lipid molecules were identified mainly situated on the cleft of the transmembrane space formed by adjacent subunits (Supplementary Fig. 5).

Overall architecture

The resolved complex exhibits an elongated shape, with dimensions of approximately 101 Å × 101 Å × 235 Å, and can be characterized as a trimer of heterotrimers, with each trimer consisting of a single copy of MmpL5, MmpS5, and AcpM (Fig. 1). The three MmpL5 subunits constitute the core of the complex, where each MmpS5 subunit is positioned between the two neighboring MmpL5 subunits, specifically its N-terminal membrane-spanning region is tightly adjacent to the transmembrane helix 8 (TMH8) of one of the MmpL5 subunits. The AcpM subunits, exposed in the cytosol, form the base of the complex. A remarkable feature of this complex is the extracellular stalk, which extends to a total length of around 130 Å and is composed of three intertwined anti-parallel coiled-coil portions of MmpL5 (Fig. 1). A total of 12 phospholipids, including six cardiolipins (CDL) and six phosphatidylethanolamines (PE), were resolved within the membrane inner leaflet of the complex (Fig. 1 and Supplementary Fig. 5). Each MmpL5 protomer harbors two distinct lipid-binding sites (Supplementary Fig. 5), one located at the surface of MmpL5 and the other within the protomer-protomer interface, specifically at the interior surface of the central cavity of the trimeric MmpL5. In addition, a PE and a CDL molecule are stacked at the interface of each MmpL5 and MmpS5, respectively (Supplementary Fig. 5). In contrast, although distinct lipid-like density patches were observed in the membrane outer leaflet, particularly at the trimeric interface, the resolution of these densities was too low to definitively identify their composition (Supplementary Fig. 5a). Nonetheless, the presence of these lipids appears to contribute to the stabilization of the membrane-spanning region of the entire complex.

The MmpL5 trimer

The structure reveals that MmpL5 subunits assemble into a symmetric homotrimer with a propeller-like configuration through a unique shoulder-to-shoulder ring-like assembly, except for the

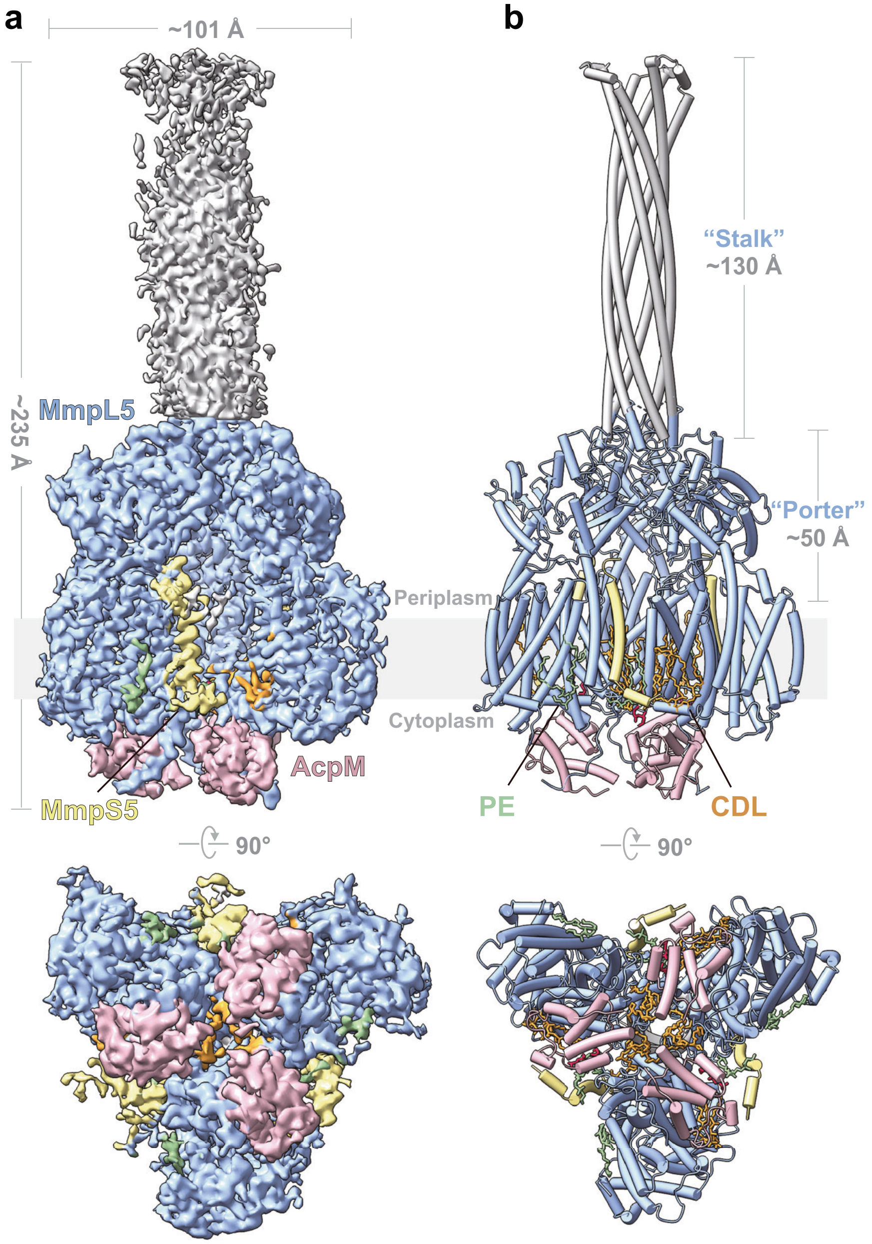

Fig. 1 | Cryo-EM structure of the MmpL5-MmpS5-AcpM complex from *Mycobacterium tuberculosis*. **a** Two views of the cryo-EM map of the MmpL5-MmpS5-AcpM complex colored by subunit (MmpL5, blue and silver; MmpS5, yellow; AcpM, pink). The volume threshold is 0.15 σ for the stalk and 0.3 σ for the other regions. **b** Cartoon representation of the MmpL5-MmpS5-AcpM complex structure from two different viewpoints. Color scheme same as in (**a**). A pseudo-atomic model of the stalk is also depicted and colored silver. Phosphatidylethanolamine (PE) and cardiolipin (CDL) molecules are shown as light green and orange sticks, respectively.

uncharacterized coiled-coil region (Fig. 2a and Supplementary Fig. 6). This assembly pattern is pronouncedly different from the well-characterized typical RND trimer such as AcrB[39], all of which are arranged in a face-to-face ring-like manner (Fig. 2a). The unique arrangement results in a smaller central cavity of the transmembrane domains within the MmpL5 trimer (Fig. 2a). To verify the trimerization of MmpL5 itself, we expressed and purified MmpL5 alone, following the same procedure as for the MmpL5/MmpS5 complex. The results showed that the isolated MmpL5 samples exhibited similar characteristics in shape and size to that of the MmpL5/MmpS5 complex in solution (Fig. 2b, c). Moreover, the in vivo occurrence of the MmpL5 trimer was validated by the introduction of cysteine substitutions designed to mediate disulfide bond formation between monomers (Fig. 2d). Thus, these findings indicate that the MmpL5 subunit ensures the trimeric form of the MmpL5/MmpS5 complex and anchors it to the membrane.

Each MmpL5 monomer consists of a 12 transmembrane α-helices (TMHs) stacked transmembrane domain (TMD) and two extracellular domains (ECDs) located between TMH1 and TMH2 (ECD1) and between TMH7 and TMH8 (ECD2), respectively, and exhibits a typical RND transporter domain organization (Fig. 2e and Supplementary Fig. 7a). Compared to other characterized RND proteins, the structure of MmpL5 monomer most closely resembles that of its paralog, the mycolic acid transporter MmpL3[37], but they differ in the extracellular regions in terms of size and shape (Fig. 2e). In both structures, ECD1 is largely similar, consisting of only one subdomain (i.e., PN) with an "open face" α + β sandwich fold. In sharp contrast, MmpL5's ECD2, in addition to a PN-like subdomain PC, has an additional insertion region

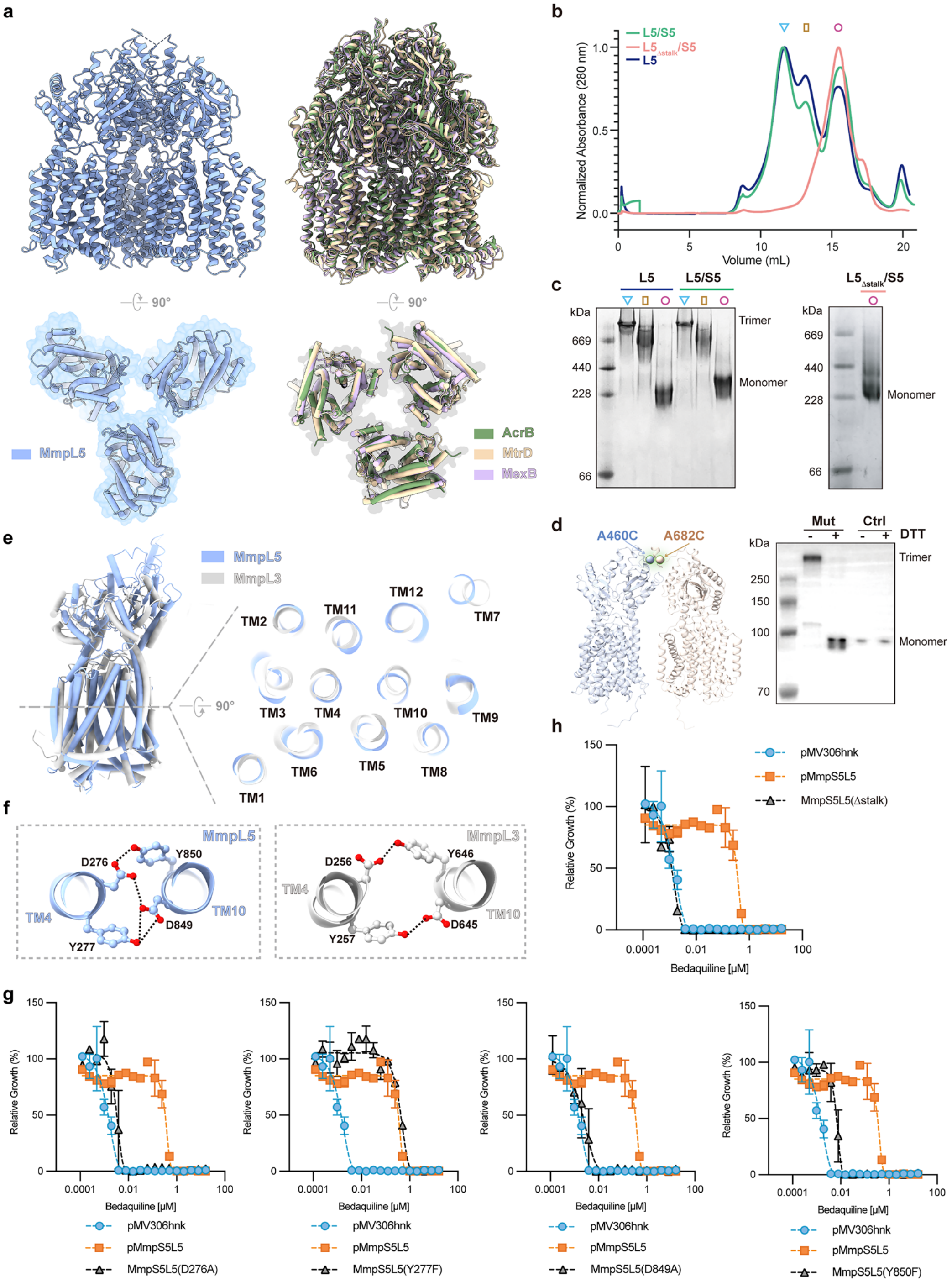

Fig. 2 | Structure and characteristics of the MmpL5 trimer. **a** Structural comparison of MmpL5 trimer with multidrug transporters AcrB (PDB code: 2DHH), MtrD (PDB code: 6VKS) and MexB (PDB code: 2V50). **b** Size exclusion chromatography (SEC) analyses of MmpL5 (L5), MmpL5/MmpS5 (L5/S5), and Stalk-truncated MmpL5/MmpS5 ($L5_{\Delta stalk}$/S5). Blue triangle, brown square and purple circle respectively indicate peaks 1, 2 and 3 in the SEC profiles. **c** BN-PAGE analyses of each peak as in (**b**). **d** Position of a pair of cysteine mutations introduced in the PC domains of MmpL5 (Left) and Western blot of the MmpL5 variant ($MmpL5_{A460C\&A682C}$, Mut) and the purified wild-type MmpL5 trimer (Ctrl) (Right). Under non-reducing conditions, a high-molecular-weight band corresponding to the MmpL5 trimer was observed in the cysteine variant but not the wild-type MmpL5. In sharp contrast, this band migrated to a smaller molecular weight under reducing conditions. In (**c**, **d**), each experiment was repeated at least three times as independent biological replicates. Source data are provided as a Source Data file. **e** Superposition of MmpL5 (blue) and MmpL3 (gray; PDB code: 6AJF) seen from the plane of the membrane (Left) and a clipped view of the transmembrane region viewed from the periplasm (Right). **f** The Asp-Tyr pairs in TM4 and TM10 of MmpL5 and MmpL3 are shown as sticks. Hydrogen bonds are indicated as dashed lines. **g**, **h** Drug susceptibility data for MmpL5 variants. Error bars correspond to mean ± SD based on two independent biological replicates. The Gompertz model was used to fit growth data. Source data are provided as a Source Data file.

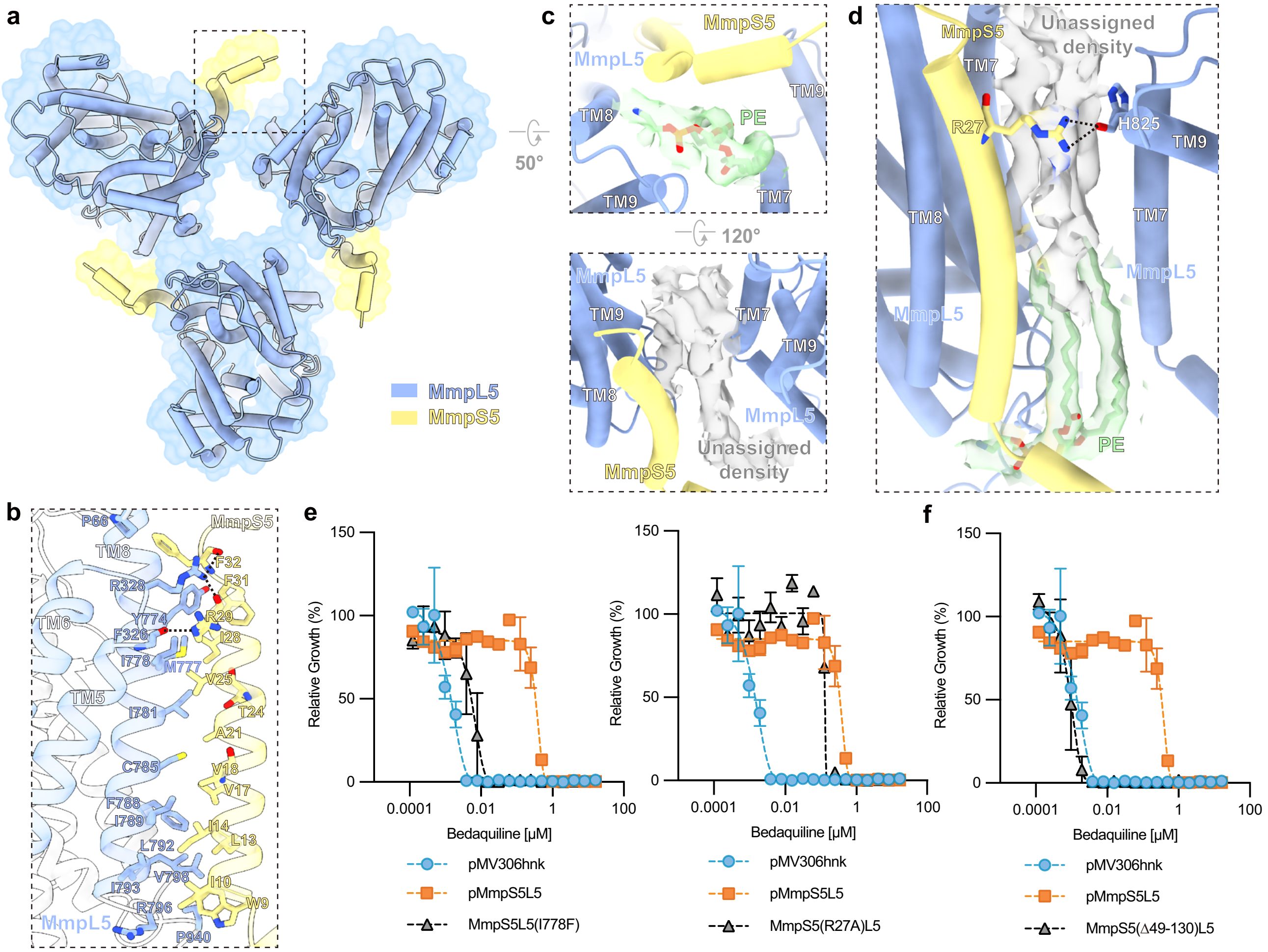

Fig. 3 | Interplay between MmpL5 and MmpS5. a The position of MmpS5 in the complex viewed from the cytoplasm. **b** Interactions between MmpS5 and MmpL5 in each protomer. Key residues are shown as sticks. Hydrogen bonds are indicated as dashed lines. **c**, **d** Close-up views of the membrane cleft between MmpS5 and two neighboring MmpL5 subunits. EM densities for PE and an unassigned ligand shown as surface with a volume threshold of 0.2 σ. The contact residues are shown as sticks. **e**, **f** Drug susceptibility data for three MmpL5/MmpS5 variants. Error bars correspond to mean ± SD based on two independent biological replicates. The Gompertz model was used to fit growth data. Source data are provided as a Source Data file.

situated between the 2nd and 3rd β-strands of PC, which is absent in MmpL3. Insertion regions are widely observed in other RND proteins, but their configurations and amino acid sequences vary (Supplementary Fig. 8), which is associated with the unique activity of each protein[40]. In MmpL5, the insertion region is primarily composed of the unmodeled coiled-coil part, implying that this region has an inherent structural flexibility relative to other regions of MmpL5. In addition, due to the closer proximity of PN and PC in MmpL5, no cavity exists resembling that observed in MmpL3, formed by the intertwined subdomains[37]. As with other characterized RND proteins, MmpL5's 12 transmembrane helices (TMH1 to TMH12) are stacked with a pseudo-two-fold symmetry, where TMH4 and TMH10 are located at the core of the transmembrane helix bundle (Fig. 2e). Two Asp-Tyr pairs (Asp276-Tyr850 and Asp849-Tyr277) of key conserved hydrophilic residues, believed to be involved in the proton-relay pathway of MmpL members[41], are situated at the middle of TMH4 and TMH10 (Fig. 2f), similar to that observed in MmpL3[37]. Significantly, three residues—Asp276, Asp849, and Tyr850—are essential for the functionality of MmpL5, whilst Tyr277 may not be needed. Specifically, Asp276 and Asp849 mutations almost completely abrogate the drug efflux activity of the MmpL5/MmpS5 complex (Fig. 2g).

MmpL5 monomer association is predominantly mediated by its ECD2, although each protomer makes contact at the cytoplasmic surface (Supplementary Fig. 7b). Intriguingly, the insertion region of MmpL5, especially the coiled-coil part, appears to provide a strong interaction holding the MmpL5s together. Notably, the removal of this part leads to the disassembly of the trimeric MmpL5/MmpS5 complex, thereby causing the loss of its efflux activity (Fig. 2b, c, h). In addition, the PC subdomains of the MmpL5 protomer contact each other through charged patches in an anti-parallel head-to-tail manner, further enhancing the stability of the trimer (Supplementary Fig. 7b). The parts of the PC subdomain in contact with each other result in a central pore with an inner diameter of around 10 Å, whose opening appears to be sealed by the bottom of the stalk, while the other parts of the PC subdomain lacking contact leave three lateral openings that could allow specific molecules to enter (Supplementary Fig. 7b).

Interface between MmpL5 and MmpS5

In the present structure, we only observed the membrane-spanning and N-terminal regions of MmpS5, which are situated at the cleft formed by two adjacent MmpL5 subunits (Fig. 3a). The single transmembrane helix of MmpS5 is parallel to the TMH8 of MmpL5 in each protomer, while its N-terminal short helix exposed to the cytosol orients to another neighboring MmpL5 subunit. Stabilization of the membrane region of MmpS5 is primarily achieved via extensive hydrophobic interactions with the TMH8 of MmpL5 (Fig. 3b). In

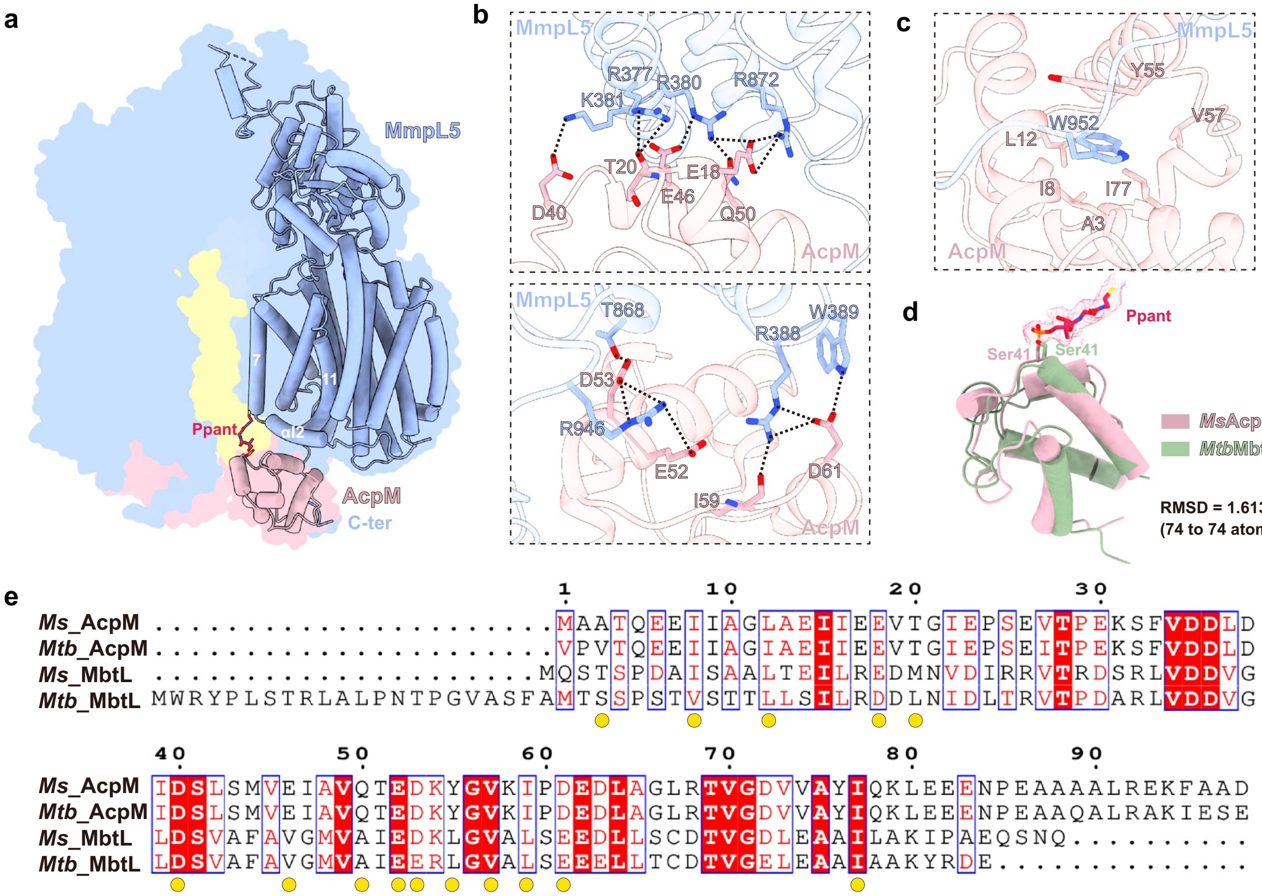

Fig. 4 | Interactions between MmpL5 and AcpM. **a** Structure of MmpL5 bound AcpM represented in cartoon and surface. 4′-phosphopantetheine (Ppant) covalently linked to AcpM is shown as red sticks. **b**, **c** Close-up views of the binding site between MmpL5 and AcpM. Key residues are shown as stick models. Hydrogen bonds and salt bridges are represented by black dashed lines. **d** Superposition of *M. smegmatis* AcpM (pink) and *M. tuberculosis* MbtL (Alphafold 2 model, light green). Ppant and the modified residue (Ser41) of AcpM are shown as stick models with the electron density displayed as mesh at a 0.2 σ threshold. **e** Sequence alignment of AcpM and MbtL from *M. smegmatis* and *M. tuberculosis*. Contacting residues at the interface are marked by yellow spheres.

addition, the loop connecting between the TMH5 and TMH6 of MmpL5 also directly interacts with MmpS5 at the periplasmic interface, participating in the stabilization of the two subunits by forming additional hydrogen bonds (Fig. 3b). It has been demonstrated that MmpS5 promotes the oligomerization of MmpL5[34], which is also corroborated by the resolved structure. In terms of the TM region, the presence of MmpS5 not only provides additional contacts with the adjacent protomers but also creates additional lipid attachment sites at the trimer interface (Fig. 3c, d).

The interplay between MmpS5 and MmpL5 is essential for the substrate efflux in this system[30,34], which is further confirmed by our study. Disruption of the transmembrane interface between these two components in the protomer severely compromises the ability of *Mtb* to resist BDQ (Fig. 3e). Functional studies on another mycobacterial siderophore exporter, MmpL4/MmpS4, have shown that the extracellular region of MmpS4 can directly contact the PN subdomain of its cognate MmpL4[30]. However, no extracellular region of MmpS5 was therefore identified in our EM maps, despite sharing approximately 63% sequence identity between MmpL5/MmpS5 and MmpL4/MmpS4, suggesting either a lower affinity or a transient contact. Interestingly, our functional data showed that the extracellular region of MmpS5 is indispensable for the functionality of the MmpS5/MmpL5 system (Fig. 3f), which underscores the importance of further exploring its exact role.

In addition to MmpL4 and MmpL5, other MmpL proteins, including MmpL1 and MmpL2 in *Mtb*, have been reported to potentially interact with their accessory proteins MmpS1 and MmpS2, respectively[33,42]. Given the highly conserved residues at the interface of the membrane-spanning regions (Supplementary Fig. 9a), it appears that the assembly mechanism of other MmpL and MmpS proteins is similar to that observed in the MmpL5/MmpS5 complex.

An unexpected binder, AcpM

AcpM, an acyl carrier protein (ACP), is well recognized for its vital role in the biosynthesis of fatty acids and mycolic acids in mycobacteria[43]. Beyond this, AcpM has also been implicated in arabinogalactan (AG) assembly or lipoarabinomannan (LAM) synthesis[44,45]. Unexpectedly, in the MmpL5/MmpS5 efflux system, the mycobacterial AcpM binds to the MmpL5 subunit at the cytoplasmic face (Fig. 4a), thus forming an MmpL5-MmpS5-AcpM ternary complex. AcpM primarily interacts with the amphiphilic helix (αI2) connecting TMH6 and TMH7 of MmpL5, as well as the cytosol-exposed portion of TMH11, and their contacts are defined largely by extensive electrostatic interactions and hydrogen bonds (Fig. 4a, b). Notably, the part of AcpM involved in this tight association is similar to the contact sites with its other target proteins, such as AcpS and Emb proteins[44,46]. Furthermore, the C-terminal loop of MmpL5 extends along the surface of AcpM to its N-terminal helix, where Trp952 on the loop wedges into a relatively hydrophobic pocket formed by six residues of AcpM (Fig. 4c), further strengthening the association of these two subunits. Of note, 4′-phosphopantetheine (Ppant), covalently attached to the conserved serine residue (Ser41) via a phosphodiester, is observed in the AcpM structure (Fig. 4a, d), indicating that AcpM is in its holo-form[44], which inserts into the gap between the two adjacent MmpL5 and phospholipid molecules.

The assembly between AcpM and MmpL5 (or an equivalent) has not been observed in any other characterized RND transporter, not even in MmpL3. During the identification of this unknown subunit, a structure-based search in the AlphaFold Protein Structure Database[47] using Foldseek[48] revealed an unresolved *Mtb* protein, MbtL (Rv1344), with a similar fold to AcpM (Fig. 4d), despite a sequence identity of only around 30% with *M. smegmatis* AcpM. MbtL is another mycobacterial ACP known to be involved in the biosynthesis of siderophores in *Mtb*[49], in the same metabolic pathway as MmpL5/MmpS5. Sequence analysis showed that the residues involved in the association with MmpL5 are relatively conserved in both AcpM and MbtL (Fig. 4e), suggesting a potential direct interplay between MbtL and MmpL5. In addition, the residues of MmpL5 involved in contact with AcpM are also conserved in MmpL4[30,33] (Supplementary Fig. 9b). Thus, this assembly pattern of MmpL5 with AcpM provides significant clues to the coupling of siderophore biosynthesis and transport in mycobacteria, warranting further investigation.

Discussion

MmpL5/MmpS5 is distinguished as the most clinically relevant multidrug efflux pump in *Mtb*. In this study, we present the previously uncharacterized structure of the MmpL5/MmpS5 complex from any source, which not only offers unprecedented insights into the assembly of the complex but also provides a foundational framework for understanding the functionality of this important efflux transporter. Moreover, the study discloses a distinctive trimer assembly pattern in the RND protein superfamily, enhancing our comprehension of the diversity and evolutionary ingenuity of these transporter structures. Notably, the MmpL5 extracellular region forms a stalk composed of coiled-coil parts, which secures the tight association of three MmpL5 subunits. The coiled-coil region's role in trimerization is analogous to the docking subdomains found in other prototypical RND multidrug efflux pumps[50], despite significant differences in shape and composition. Given that MmpL proteins in Cluster I all possess a coiled-coil structure (Supplementary Fig. 1), we suggest that other members of this cluster may also assemble into functional MmpL5-like trimers. Moreover, this study serves as a paradigm for understanding the biological assembly of other MmpL proteins and their accessory MmpS proteins across *Mycobacterium* species.

It has been documented that the MmpL5/MmpS5 efflux transporter resembles the AcrAB-TolC system, a typical tripartite efflux pump of Gram-negative bacteria, where MmpL5 and MmpS5 respectively correspond to the inner membrane transporter AcrB and the periplasmic adapter protein AcrA, although the identity of the outer membrane channel equivalent to TolC remains elusive[34]. Structural comparisons indicate that the stalk of MmpL5/MmpS5 seems to extend to a position analogous to that of AcrA in the AcrAB-TolC system (Supplementary Fig. 10), where AcrA primarily serves to connect AcrB to TolC[50]. However, due to the distinct location and structural divergence, MmpS5 is unlikely to function as an adapter linking MmpL5 to an unidentified outer membrane channel as AcrA does. Thus, whether the stalk of MmpL5/MmpS5 connects to a potential outer membrane channel or mediates substrate transport across the periplasmic space awaits further investigation.

Unlike the classical multidrug efflux transporter AcrB[51], MmpL5 lacks periplasmic clefts between the PN and PC subdomains and does not possess proximal and distal substrate binding sites. Consequently, the MmpL5/MmpS5 system does not appear to capture drugs from the periplasm in the same manner as AcrB. Instead, the transmembrane gap between MmpS5 and the two adjacent MmpL5 subunits may serve as a potential binding pocket for hydrophobic drugs, including BDQ (Supplementary Fig. 10c). This pocket allows access from either the outer or inner leaflet of the membrane, as observed in the resolved structure, although the pocket is occupied by endogenous lipids. We also surmise that the physiological substrates, such as (carboxy) mycobactins, are likely captured by the MmpL5/MmpS5 system through this gap after synthesis. This hypothesis is supported by the presence of a large hydrophobic molecule-binding patch adjacent to the entrance of the membrane inner leaflet, namely the CDL binding site, which is conducive to capturing the relatively hydrophobic segments of (carboxy)mycobactins[52]. In addition, residues in MmpL5 that may be involved in the association of MbtL are located near this entrance.

In terms of substrate transport, the multidrug exporter AcrB extrudes drugs/substrates via a functionally rotating mechanism[53], where each protomer adopts distinct configurations, namely binding/tight, access/loose and extrusion/open. In this study, the MmpL5/MmpS5 structure we determined is a symmetric trimer, a characteristic also observed in other trimeric RND transporters, including AcrB, in their resting state[54,55], which is deemed likely to be due to the absence of bound substrates or additional components such as outer membrane channels or accessory subunits[56–58]. The details of substrate transport mediated by the MmpL5/MmpS5 system therefore require further elucidation. In conclusion, the investigation significantly deepens our understanding of the structure and function of MmpL5/MmpS5 and, in so doing, other MmpL family members, and will facilitate the discovery of innovative inhibitors that target these systems.

Methods

Cloning and expression

The genes *mmpS5-mmpL5* (*Rv0677c-Rv0676c*) encoding MmpL5/MmpS5 complex were cloned from the genomic DNA of *Mycobacterium tuberculosis* strain H37Rv, and subsequently inserted into the pMV261 vector, fused with a C-terminal 1 × FLAG tag attached to MmpL5. The recombinant plasmid, verified by sequencing, was then transformed into *Mycobacterium smegmatis* MC^{2}155 cells using electroporation. The transformed cells were cultivated at 37 °C in Luria Broth (LB) liquid media supplemented with 50 µg/mL kanamycin, 20 µg/mL carbenicillin and 0.1% (v/v) Tween 80, and were induced with 0.2% (w/v) acetamide (final concentration) at 16 °C when the OD_{600} reached 1.0. Cells were harvested after four days and frozen at − 80 °C. All site-directed mutant plasmids, as well as a plasmid harboring a truncated coiled-coil region of MmpL5, were generated using standard PCR methods. Each of these constructs was overexpressed following the same protocol as the wild-type MmpL5/MmpS5. The sequences of primers used for cloning and related materials are provided in Supplementary Data 1–3.

Protein purification

Cell pellets were thawed and resuspended in the buffer containing 20 mM HEPES at pH 7.5, and 150 mM NaCl. Disruption of cells was achieved using a high-pressure homogenizer operated at 1200 bar. Subsequent removal of cell debris was facilitated by centrifugation at 14,000 × *g* for 15 min at 4 °C. The supernatant was further applied to ultracentrifugation at 150,000 × *g* for 1.5 h. The fractions were then resuspended in an extraction buffer containing 50 mM HEPES at pH 7.5, 150 mM NaCl, and 1% (w/v) DDM (D310, Anatrace), incubated at 4 °C for 1.5 h, and subsequently centrifuged at 20,000 × *g* for 45 min. The supernatant was loaded onto an anti-DYKDDDDK affinity resin (GenScript) column, and washed with buffer containing 20 mM HEPES at pH 7.5, 150 mM NaCl, and 0.04% (w/v) GDN (GDN-101, Anatrace). Target proteins were eluted using an elution buffer composed of 20 mM HEPES at pH 7.5, 150 mM NaCl, 0.2 mg/mL FLAG peptides (Sigma-Aldrich) and 0.04% (w/v) GDN. After concentration, proteins underwent further purification through size exclusion chromatography on a Superose 6 Increase 10/300 GL column from GE Healthcare, using a running buffer containing 20 mM HEPES at pH 7.5, 150 mM NaCl, 2 mM DTT, and 0.04% (w/v) GDN. The peak fractions were pooled and concentrated to a final concentration of 5 mg/mL for cryo-EM sample preparation.

Cryo-EM sample preparation and data collection

3 µL aliquots of concentrated samples were applied to glow-discharged holey carbon grids (Quantifoil Au R0.6/1.0, 300 mesh). The glow discharge was conducted following a standard mixture of hydrogen and oxygen gases. Grids were blotted for 3 s and then rapidly plunge-frozen in liquid ethane, which was cooled by liquid nitrogen, using a Vitrobot Mark IV (ThermoFisher Scientific) at 8 °C and 100% humidity. Grids were then transferred to a Titan Krios electron microscope (ThermoFisher Scientific) operating at 300 keV. The microscope was equipped with a Gatan Gif Quantum energy filter and a spherical aberration (Cs) image corrector. Micrographs were recorded using a K3 Summit direct electron detector (Gatan Company) in super-resolution mode, with a nominal magnification of 105,000 ×, yielding a calibrated pixel size of 0.832 Å. Each micrograph was exposed for 2 s, with a total dose of around 60 $e^-/Å^2$ and 40 dose-fractionated frames. SerialEM software was employed for fully automated data collection[59]. The defocus values were set, ranging from −1.2 to −1.8 µm.

Image processing

8961 cryo-EM micrographs were collected and subjected to beam-induced motion correction with MotionCor2[60]. Subsequent processing steps were performed using cryoSPARC[61]. After contrast transfer function (CTF) estimation, micrographs exhibiting poor quality, such as those with high astigmatism, low CTF fit resolution, and large-offset defocus values, were manually discarded. From the selected micrographs, 2,985,321 particles were automatically picked and extracted with a box size of 384 pixels. Reference-free 2D classification was performed to eliminate ice spots, contaminants, and aggregates, yielding a refined set of 149,391 particles. The particles were then used for ab-initio reconstruction to generate initial 3D volumes, which served as templates for heterogeneous refinement. This process led to the generation of a high-quality 3D volume containing 83,178 particles, which was then underwent homogeneous refinement, followed by non-uniform and local refinement. Ultimately, density maps imposed with C1 and C3 symmetry were obtained, with estimated average resolutions of 2.84 Å (map-1) and 2.64 Å (map-2), respectively, based on the gold-standard Fourier shell correlation (FSC) cut-off of 0.143[62]. To generate a map that included the stalk region, a consensus set of particles was used for 3D classification. Particles from the selected 3D classification class were subjected to re-2D classification to remove bad particles. Particles from the chosen 2D classes were re-extracted with a box size of 512 pixels (unbinned) and refined using homogeneous and non-uniform refinement to generate the maps that encompassed the entire complex. The final density maps, with imposed C1 and C3 symmetry, had estimated average resolutions of 3.31 Å (map-3) and 2.95 Å (map-4), respectively, again based on the FSC cut-off of 0.143. Local resolution ranges were analyzed in cryoSPARC. Detailed numbers and processing steps are presented in Supplementary Fig. 3.

Model building and refinement

The predicted models of MmpL5 and MmpS5, generated by AlphaFold2[47], were docked into the cryo-EM density maps in UCSF ChimeraX[63] and subsequently manually refined in Coot[64]. To uncover the unidentified subunit, the Cα backbone of the polypeptide was manually traced in Coot, and then these coordinates were used to perform a structure-based search in the Protein Data Bank and AlphaFold Protein Structure Database[47]. Among the top-ranking results from these searches, an acyl carrier protein, AcpM, from *Mycobacterium smegmatis* (MSMEG_4326), emerged with a TM-score of 0.889. After minimal adjustments, the structure of *Mycobacterium smegmatis* AcpM (PDB ID: 7BVE) was found to align well with the cryo-EM density, confirming its identity. Multiple cycles of real-space refinement were conducted in PHENIX[65] to optimize the models' fit to the density maps. The models were evaluated using MolProbity[66]. Cryo-EM data collection and model refinement statistics are shown in Supplementary Table 1. All graphics were generated using PyMOL (www.pymol.org) or UCSF ChimeraX.

Blue Native PAGE

Chromatographically purified samples of MmpL5/MmpS5, MmpL5 and Stalk-truncated MmpL5/MmpS5 were respectively mixed with glycerol to a final concentration of 20%. These samples were subsequently loaded onto 4–16% NativePAGE™ Bis-Tris Gel (Invitrogen) and subjected to electrophoresis at a constant voltage of 150 V for a duration of 2 h at 4 °C. All buffer conditions and procedures were based on a previously published Blue Native PAGE protocol[67].

Structure-guided disulfide cross-bridge experiment

To determine the natural oligomeric configuration of MmpL5, a search for engineering the insertion of a stabilizing disulfide bridge was conducted. We isolated cell membranes from *Mycobacterium smegmatis* MC^{2}155 expressing *Mycobacterium tuberculosis* MmpL5 with the strategic cysteine substitutions ($\mathrm{MmpL5_{A460C\&A682C}}$), and established a parallel control with the purified wild-type MmpL5. Protein samples were treated with loading buffer containing sodium dodecyl sulfate (SDS), either with or without the reducing agent dithiothreitol (DTT). Following electrophoresis, the proteins were transferred onto a polyvinylidene difluoride (PVDF) membrane. The membrane was then blocked with TBST buffer [20 mM Tris-HCl (pH 8.0), 150 mM NaCl, and 0.05% Tween 20] supplemented with 5% skim milk at room temperature for 2 h. Subsequently, the PVDF membranes were incubated with anti-FLAG antibody (1:10,000) (catalog no. 66008 from Proteintech with validation data available on the manufacturer's website) at 4 °C overnight. The PVDF membranes were then thoroughly washed three times with TBST buffer and incubated with Multi-rAb horseradish peroxidase (HRP)-conjugated goat anti-mouse secondary antibody (1:10,000) (RGAM001, Proteintech) at room temperature for 1 h. Finally, the PVDF membranes were developed using an ECL Light Chemiluminescence Kit (Epizyme) to visualize the immunoreactive bands.

Drug susceptibility assay

Mycobacterium tuberculosis mmpS5-mmpL5 (*mmpS5L5*) deletion mutant was constructed using mycobacterial recombineering as previously described[68]. The *mmpS5L5* open reading frame was designed to be expressed from the Hsp60 promoter of pMV306HNK, a derivative of pMV306[69]. The resulting plasmid, pMBM12, was synthesized and cloned at GenScript. All variants of MmpL5/MmpS5 were constructed by GenScript using their mutagenesis protocol. All plasmids were transformed into Δ*mmpS5L5*::hyg using previously described protocols[70,71]. All colonies were screened for bedaquiline susceptibility using previously described compound susceptibility assays[72]. Briefly, inner wells (rows B–G, columns 3–11) of a 96-well flat-bottomed microtiter plate (ThermoFisher Scientific) were filled with 75 µL 7H9 media. Outer wells were filled with 150 µL 7H9 media as media only controls, and 75 µL of 7H9 media containing compound of interest was added to column 2 of rows B–G. Compound was diluted 2-fold, by transferring 75 µL between wells, down to column 10. Dilution continued across two 96-well plates to give a 20-point dilution curve. Column 11 on both plates was kept as solvent only. Strains were diluted to an OD_{600} of 0.01. 75 µL of diluted culture was added to inner wells of the 96-well flat-bottomed microtiter plate containing compound to achieve a starting OD_{600} of 0.005 in a final volume of 150 µL. Plates were incubated at 37 °C for 10 days without shaking. After 10 days, plates were covered with plate seals, shaken for 1 min and the OD_{600} was determined using a Varioskan Flash microplate reader (ThermoFisher Scientific). OD_{600} reads from duplicate plates were corrected for background, and values relative to the growth of the no compound control were analyzed using a nonlinear fitting of data to the Gompertz equation[73]. The list of plasmids and the sequences of oligos used in this experiment are available in Supplementary Data 1–3. All images were generated using GraphPad Prism 10.2.3 (https://www.graphpad.com).

Reporting summary

Further information on research design is available in the Nature Portfolio Reporting Summary linked to this article.

Data availability

The 3D cryo-EM density maps have been deposited in the Electron Microscopy Data Bank (EMDB) and assigned the accession numbers EMD-60202, EMD-60203, EMD-60204 and EMD-60205. The atomic coordinates for the *Mtb* MmpL5-MmpS5-AcpM structure have been deposited in the Protein Data Bank (PDB) under the identification codes 8ZKP and 8ZKQ. PDB codes of previously published structures used in this study are 7BVE, 2DHH, 6VKS, 2V50, 7NVH, 6AJF, 3AQP, 5KHN, 1IWG and 5V5S. Source data are provided in this paper.

References

1. WHO. *Global Tuberculosis Report 2024* (2024).
2. Dheda, K. et al. The Lancet Respiratory Medicine Commission: 2019 update: epidemiology, pathogenesis, transmission, diagnosis, and management of multidrug-resistant and incurable tuberculosis. *Lancet Respir. Med.* **7**, 820–826 (2019).
3. Velayati, A. A. et al. Differences in cell wall thickness between resistant and nonresistant strains of Mycobacterium tuberculosis: using transmission electron microscopy. *Chemotherapy* **55**, 303–307 (2009).
4. Howard, N. C. et al. Mycobacterium tuberculosis carrying a rifampicin drug resistance mutation reprograms macrophage metabolism through cell wall lipid changes. *Nat. Microbiol.* **3**, 1099–1108 (2018).
5. Liu, Q. et al. Mycobacterium tuberculosis clinical isolates carry mutational signatures of host immune environments. *Sci. Adv.* **6**, eaba4901 (2020).
6. Draker, K. A., Boehr, D. D., Elowe, N. H., Noga, T. J. & Wright, G. D. Functional annotation of putative aminoglycoside antibiotic modifying proteins in Mycobacterium tuberculosis H37Rv. *J. Antibiot.***56**, 135–142 (2003).
7. Xu, Y., Zhang, Z. & Sun, Z. Drug resistance to Mycobacterium tuberculosis: from the traditional Chinese view to modern systems biology. *Crit. Rev. Microbiol.* **41**, 399–410 (2015).
8. Sonnenkalb, L. et al. Bedaquiline and clofazimine resistance in Mycobacterium tuberculosis: an in-vitro and in-silico data analysis. *Lancet Microbe* **4**, e358–e368 (2023).
9. Riviere, E. et al. Variants in bedaquiline-candidate-resistance genes: Prevalence in bedaquiline-naive patients, effect on MIC, and association with Mycobacterium tuberculosis Lineage. *Antimicrob. Agents Chemother.* **66**, e0032222 (2022).
10. Saeed, D. K. et al. Variants associated with Bedaquiline (BDQ) resistance identified in Rv0678 and efflux pump genes in Mycobacterium tuberculosis isolates from BDQ naive TB patients in Pakistan. *BMC Microbiol.* **22**, 62 (2022).
11. Cohen, J. Infectious disease. Approval of novel TB drug celebratedwith restraint. *Science* **339**, 130 (2013).
12. Andries, K. et al. A diarylquinoline drug active on the ATP synthase of Mycobacterium tuberculosis. *Science* **307**, 223–227 (2005).
13. Guo, H. et al. Structure of mycobacterial ATP synthase bound to the tuberculosis drug bedaquiline. *Nature* **589**, 143–147 (2021).
14. Preiss, L. et al. Structure of the mycobacterial ATP synthase Fo rotor ring in complex with the anti-TB drug bedaquiline. *Sci. Adv.* **1**, e1500106 (2015).
15. Veziris, N. et al. Rapid emergence of Mycobacterium tuberculosis bedaquiline resistance: lessons to avoid repeating past errors. *Eur. Respir. J.* **49**, https://doi.org/10.1183/13993003.01719-2016 (2017).
16. de Vos, M. et al. Bedaquiline Microheteroresistance after Cessation of Tuberculosis treatment. *N. Engl. J. Med.* **380**, 2178–2180 (2019).
17. Somoskovi, A., Bruderer, V., Homke, R., Bloemberg, G. V. & Bottger, E. C. A mutation associated with clofazimine and bedaquiline cross-resistance in MDR-TB following bedaquiline treatment. *Eur. Respir. J.* **45**, 554–557 (2015).
18. Bloemberg, G. V. et al. Acquired resistance to bedaquiline and delamanid in therapy for tuberculosis. *N. Engl. J. Med.* **373**, 1986–1988 (2015).
19. Walker, T. M. et al. The 2021 WHO catalogue of Mycobacterium tuberculosis complex mutations associated with drug resistance: A genotypic analysis. *Lancet Microbe* **3**, e265–e273 (2022).
20. Kadura, S. et al. Systematic review of mutations associated with resistance to the new and repurposed Mycobacterium tuberculosis drugs bedaquiline, clofazimine, linezolid, delamanid and pretomanid. *J. Antimicrob. Chemother.* **75**, 2031–2043 (2020).
21. Radhakrishnan, A. et al. Crystal structure of the transcriptional regulator Rv0678 of Mycobacterium tuberculosis. *J. Biol. Chem.* **289**, 16526–16540 (2014).
22. Xu, J. et al. Primary clofazimine and bedaquiline resistance among isolates from patients with multidrug-resistant tuberculosis. *Antimicrob. Agents Chemother.* **61**, https://doi.org/10.1128/AAC.00239-17 (2017).
23. Peretokina, I. V. et al. Reduced susceptibility and resistance to bedaquiline in clinical M. tuberculosis isolates. *J. Infect.* **80**, 527–535 (2020).
24. Liu, Y. et al. Reduced Susceptibility of Mycobacterium tuberculosis to bedaquiline during antituberculosis treatment and its correlation with clinical outcomes in China. *Clin. Infect. Dis.* **73**, e3391–e3397 (2021).
25. Nimmo, C. et al. Population-level emergence of bedaquiline and clofazimine resistance-associated variants among patients with drug-resistant tuberculosis in southern Africa: a phenotypic and phylogenetic analysis. *Lancet Microbe* **1**, e165–e174 (2020).
26. Villellas, C. et al. Unexpected high prevalence of resistance-associated Rv0678 variants in MDR-TB patients without documented prior use of clofazimine or bedaquiline. *J. Antimicrob. Chemother.* **72**, 684–690 (2017).
27. Hartkoorn, R. C., Uplekar, S. & Cole, S. T. Cross-resistance between clofazimine and bedaquiline through upregulation of MmpL5 in Mycobacterium tuberculosis. *Antimicrob. Agents Chemother.* **58**, 2979–2981 (2014).
28. Van Deun, A. et al. Short, highly effective, and inexpensive standardized treatment of multidrug-resistant tuberculosis. *Am. J. Respir. Crit. Care Med.* **182**, 684–692 (2010).
29. Piddock, L. J. Multidrug-resistance efflux pumps - not just for resistance. *Nat. Rev. Microbiol.* **4**, 629–636 (2006).
30. Wells, R. M. et al. Discovery of a siderophore export system essential for virulence of Mycobacterium tuberculosis. *PLoS Pathog.* **9**, e1003120 (2013).
31. De Voss, J. J. et al. The salicylate-derived mycobactin siderophores of Mycobacterium tuberculosis are essential for growth in macrophages. *Proc. Natl. Acad. Sci. USA* **97**, 1252–1257 (2000).
32. Briffotaux, J., Huang, W., Wang, X. & Gicquel, B. MmpS5/MmpL5 as an efflux pump in Mycobacterium species. *Tuberculosis* **107**, 13–19 (2017).

33. Cole, S. T. et al. Deciphering the biology of Mycobacterium tuberculosis from the complete genome sequence. *Nature* **393**, 537–544 (1998).
34. Yamamoto, K., Nakata, N., Mukai, T., Kawagishi, I. & Ato, M. Coexpression of MmpS5 and MmpL5 contributes to both efflux transporter MmpL5 trimerization and drug resistance in Mycobacterium tuberculosis. *mSphere* **6**, https://doi.org/10.1128/mSphere.00518-20 (2021).
35. Viljoen, A. et al. The diverse family of MmpL transporters in mycobacteria: from regulation to antimicrobial developments. *Mol. Microbiol.* **104**, 889–904 (2017).
36. Chim, N. et al. The structure and interactions of periplasmic domains of crucial MmpL membrane proteins from Mycobacterium tuberculosis. *Chem. Biol.* **22**, 1098–1107 (2015).
37. Zhang, B. et al. Crystal structures of membrane transporter MmpL3, an anti-TB drug target. *Cell* **176**, 636–648 (2019).
38. Su, C. C. et al. MmpL3 is a lipid transporter that binds trehalose monomycolate and phosphatidylethanolamine. *Proc. Natl. Acad. Sci. USA* **116**, 11241–11246 (2019).
39. Klenotic, P. A., Moseng, M. A., Morgan, C. E. & Yu, E. W. Structural and functional diversity of resistance-nodulation-cell division transporters. *Chem. Rev.* **121**, 5378–5416 (2021).
40. Zhang, Y. et al. Structural basis for cholesterol transport-like activity of the hedgehog receptor patched. *Cell* **175**, 1352–1364 (2018).
41. Bernut, A. et al. Insights into the smooth-to-rough transitioning in Mycobacterium bolletii unravels a functional Tyr residue conserved in all mycobacterial MmpL family members. *Mol. Microbiol.* **99**, 866–883 (2016).
42. Chalut, C. MmpL transporter-mediated export of cell-wall associated lipids and siderophores in mycobacteria. *Tuberculosi***100**, 32–45 (2016).
43. Kremer, L. et al. Biochemical characterization of acyl carrier protein (AcpM) and malonyl-CoA:AcpM transacylase (mtFabD), two major components of Mycobacterium tuberculosis fatty acid synthase II. *J. Biol. Chem.* **276**, 27967–27974 (2001).
44. Zhang, L. et al. Structures of cell wall arabinosyltransferases with the anti-tuberculosis drug ethambutol. *Science* **368**, 1211–1219 (2020).
45. Tan, Y. Z. et al. Cryo-EM structures and regulation of arabinofuranosyltransferase AftD from Mycobacteria. *Mol. Cell* **78**, 683–699 (2020).
46. Parris, K. D. et al. Crystal structures of substrate binding to Bacillus subtilis holo-(acyl carrier protein) synthase reveal a novel trimeric arrangement of molecules resulting in three active sites. *Structure* **8**, 883–895 (2000).
47. Varadi, M. et al. AlphaFold protein structure database: Massively expanding the structural coverage of protein-sequence space with high-accuracy models. *Nucleic Acids Res.* **50**, D439–D444 (2022).
48. van Kempen, M. et al. Fast and accurate protein structure search with Foldseek. *Nat. Biotechnol.* **42**, 243–246 (2024).
49. Shyam, M. et al. The Mycobactin biosynthesis pathway: A prospective therapeutic target in the battle against tuberculosis. *J. Med. Chem.* **64**, 71–100 (2021).
50. Klenotic, P. A. & Yu, E. W. Structural analysis of resistance-nodulation cell division transporters. *Microbiol. Mol. Biol. Rev.* **88**, https://doi.org/10.1128/mmbr.00198-23 (2024).
51. Nakashima, R., Sakurai, K., Yamasaki, S., Nishino, K. & Yamaguchi, A. Structures of the multidrug exporter AcrB reveal a proximal multisite drug-binding pocket. *Nature* **480**, 565–569 (2011).
52. Arnold, F. M. et al. The ABC exporter IrtAB imports and reduces mycobacterial siderophores. *Nature* **580**, 413–417 (2020).
53. Murakami, S., Nakashima, R., Yamashita, E., Matsumoto, T. & Yamaguchi, A. Crystal structures of a multidrug transporter reveal a functionally rotating mechanism. *Nature* **443**, 173–179 (2006).
54. Murakami, S., Nakashima, R., Yamashita, E. & Yamaguchi, A. Crystal structure of bacterial multidrug efflux transporter AcrB. *Nature* **419**, 587–593 (2002).
55. Zhang, Z., Morgan, C. E., Cui, M. & Yu, E. W. Cryo-EM structures of AcrD illuminate a mechanism for capturing aminoglycosides from its central cavity. *mBio* **14**, e0338322 (2023).
56. Wang, Z. et al. An allosteric transport mechanism for the AcrAB-TolC multidrug efflux pump. *Elife* **6**, https://doi.org/10.7554/eLife.24905 (2017).
57. Tsutsumi, K. et al. Structures of the wild-type MexAB-OprM tripartite pump reveal its complex formation and drug efflux mechanism. *Nat. Commun.* **10**, 1520 (2019).
58. Su, C. C. et al. Cryo-electron microscopy structure of an Acinetobacter baumannii multidrug efflux pump. *mBio* **10**, https://doi.org/10.1128/mBio.01295-19 (2019).
59. Mastronarde, D. N. Automated electron microscope tomography using robust prediction of specimen movements. *J. Struct. Biol.* **152**, 36–51 (2005).
60. Zheng, S. Q. et al. MotionCor2: anisotropic correction of beam-induced motion for improved cryo-electron microscopy. *Nat. Methods* **14**, 331–332 (2017).
61. Punjani, A., Rubinstein, J. L., Fleet, D. J. & Brubaker, M. A. cryoSPARC: algorithms for rapid unsupervised cryo-EM structure determination. *Nat. Methods* **14**, 290–296 (2017).
62. Grigorieff, N. Frealign: An Exploratory Tool for Single-Particle Cryo-EM. *Methods Enzymol.* **579**, 191–226 (2016).
63. Goddard, T. D. et al. UCSF ChimeraX: Meeting modern challenges in visualization and analysis. *Protein Sci.* **27**, 14–25 (2018).
64. Emsley, P., Lohkamp, B., Scott, W. G. & Cowtan, K. Features and development of Coot. *Acta Crystallogr. D Biol. Crystallogr.* **66**, 486–501 (2010).
65. Adams, P. D. et al. PHENIX: a comprehensive Python-based system for macromolecular structure solution. *Acta Crystallogr. D Biol. Crystallogr.* **66**, 213–221 (2010).
66. Chen, V. B. et al. MolProbity: all-atom structure validation for macromolecular crystallography. *Acta Crystallogr. D Biol. Crystallogr.* **66**, 12–21 (2010).
67. Wittig, I., Braun, H. P. & Schagger, H. Blue native PAGE. *Nat. Protoc.* **1**, 418–428 (2006).
68. Murphy, K. C. et al. ORBIT: a New Paradigm for Genetic Engineering of Mycobacterial Chromosomes. *mBio* **9**, https://doi.org/10.1128/mBio.01467-18 (2018).
69. Wang, Q. et al. PE/PPE proteins mediate nutrient transport across the outer membrane of Mycobacterium tuberculosis. *Science* **367**, 1147–1151 (2020).
70. Wang, X. et al. Whole genome CRISPRi screening identifies druggable vulnerabilities in an isoniazid resistant strain of Mycobacterium tuberculosis. *Nat. Commun.* **15**, 9791 (2024).
71. Adolph, C. et al. A dual-targeting succinate dehydrogenase and F(1)F(o)-ATP synthase inhibitor rapidly sterilizes replicating and non-replicating Mycobacterium tuberculosis. *Cell Chem. Biol.* **31**, 683–698 (2024).
72. Waller, N. J. E., Cheung, C. Y., Cook, G. M. & McNeil, M. B. The evolution of antibiotic resistance is associated with collateral drug phenotypes in Mycobacterium tuberculosis. *Nat. Commun.* **14**, 1517 (2023).
73. Lambert, R. J. & Pearson, J. Susceptibility testing: accurate and reproducible minimum inhibitory concentration (MIC) and non-inhibitory concentration (NIC) values. *J. Appl. Microbiol.* **88**, 784–790 (2000).

Acknowledgements

We extend our sincere gratitude to the staff at the Electron Microscopy Facility of ShanghaiTech University and the Mass Spectrometry System at the National Facility for Protein Science in Shanghai, Zhangjiang Lab, China, for their invaluable assistance during data collection. Our appreciation also goes to the Analytical chemistry platform at Shanghai Institute for Advanced Immunochemical Studies. This work was supported by grants from the National Natural Science Foundation of China (Grant Nos. 32394010 to Z.R., 32171217 and 32394011 to B.Z.), Shanghai Rising-Star Program (Grant No. 24QA2705700 to B.Z.), Major Project of Guangzhou National Laboratory (Grant No. GZNL2024A01024 to B.Z.), Shenzhen High-level Hospital Construction Fund (Grant No. 23264G1001 to Y.Z.) and the Shanghai Frontiers Science Center for Biomacromolecules and Precision Medicine, ShanghaiTech University.

Author contributions

B.Z. and Z.R. were responsible for the conception, initiation, and overall coordination of the project. Z.X. expertly managed the purification of the proteins and the preparation of cryo-EM samples, as well as the collection and processing of cryo-EM data. B.Z. and Z.X. collaborated on building and refining the structure models. Z.X. with the invaluable assistance of S.W., T.H., Y.R., C.X., Z.L., Xiuna Yang and Y.Z., conducted the biochemical experiments. C.J.S. and H.M.S. performed drug susceptibility experiments with help from W.J.J., G.M.C., and M.B.M. The manuscript was crafted by B.Z., Z.X., Xiaolin Yang, L.W.G., and Z.R. with significant contributions from all authors.

Competing interests

The authors declare no competing interests.

Additional information

Supplementary information The online version contains supplementary material available at https://doi.org/10.1038/s41467-025-60365-5.

Correspondence and requests for materials should be addressed to Zihe Rao or Bing Zhang.

Peer review information *Nature Communications* thanks Xiaodi Tang and the other anonymous reviewer(s) for their contribution to the peer review of this work. A peer review file is available.

Reprints and permissions information is available at http://www.nature.com/reprints